

Journal of Materials Chemistry B

Accepted Manuscript



This is an *Accepted Manuscript*, which has been through the Royal Society of Chemistry peer review process and has been accepted for publication.

Accepted Manuscripts are published online shortly after acceptance, before technical editing, formatting and proof reading. Using this free service, authors can make their results available to the community, in citable form, before we publish the edited article. We will replace this *Accepted Manuscript* with the edited and formatted *Advance Article* as soon as it is available.

You can find more information about *Accepted Manuscripts* in the [Information for Authors](#).

Please note that technical editing may introduce minor changes to the text and/or graphics, which may alter content. The journal's standard [Terms & Conditions](#) and the [Ethical guidelines](#) still apply. In no event shall the Royal Society of Chemistry be held responsible for any errors or omissions in this *Accepted Manuscript* or any consequences arising from the use of any information it contains.

Cite this: DOI: 10.1039/c0xx00000x

www.rsc.org/xxxxxx

ARTICLE TYPE

One-step hydrothermal synthesis of Fe₃O₄@C nanoparticles with great performance in biomedicineGui-Yun Mao^a, Wen-Jing Yang^b, Fan-Xing Bu^a, Dong-Mei Jiang^a, Zhen-Jie Zhao^a, Qing-Hong Zhang^c, Qi-Chen Fang^{b*}, Ji-Sen Jiang^{a*}

5 Received (in XXX, XXX) Xth XXXXXXXXX 20XX, Accepted Xth XXXXXXXXX 20XX

DOI: 10.1039/b000000x

Core-shell structured Fe₃O₄@C nanoparticles were fabricated by a facile one-pot hydrothermal route. The structure and component of the nanoparticles were fully characterized by transmission electron microscope, X-ray diffraction, Mössbauer spectroscopy, Raman spectroscopy, thermogravimetric analysis, magnetometry and Brunauer–Emmett–Teller specific surface area measurement. The obtained Fe₃O₄@C nanoparticles possessed favorable dispersibility, high saturation magnetization (61.4 emu g⁻¹) that could quickly response to external magnetic field and excellent biocompatibility. Excitingly, the experiments of the Fe₃O₄@C nanoparticles as drug carriers revealed an efficient drug-loading as high as 1.08 mg mg⁻¹. More importantly, the drug loading composite exhibited pH-responsive release profiles and the duration was as long as 200 h, at the pH value of 5.8 and 7.4, the release rate was 93.7% and 33.6%, respectively. Furthermore, the resulted Fe₃O₄@C nanoparticles had good magneto-thermal ability. All these positive attributes make the as-prepared Fe₃O₄@C nanoparticles a promising platform for further biomedical evaluations.

Introduction

20 In recent decades, nanotechnology has received considerable attention for their unique characteristics and has gained tremendous success by joining together with biology, medicine or other disciplines.^{1,2} Rapid development has been achieved on the nanomaterials' application to biomedicine especially cancer therapy in the past years, and extensive research has been focused on nanoparticles.^{3,4} Magnetic nanoparticles have become the recent research center for their attractive properties which portend potential biomedical applications, such as contrast agents for magnetic resonance imaging (MRI), targeted drug/gene/RNA delivery, hyperthermia, biomolecular separation and purification.⁵⁻⁸ Among those, Fe₃O₄ is the most promising candidate because it has been proved to have good stability, low cytotoxicity, and high magnetic saturation for excellent magnetic operation.^{9,10} For better biocompatibility and multiple-levels functions, various modification of Fe₃O₄ are often necessary.¹¹ For example, liposome, micelle, polymer, dendrimers, silica, carbon have been widely used for synthesis magnetic composites with good biocompatibility.¹²⁻¹⁶ Forming composites with carbon has been a major approach, since the carbon moiety may reduce aggregation, protect the core from oxidation, and increase surface area to promote drug loading content. The most widely used methods up to now is in-situ modification during the synthesis of Fe₃O₄, or using some decorates after obtaining the magnetic particles.¹⁷ Generally, such composites were synthesized by mixing magnetic nanoparticles or their precursors with carbon source (e.g., glucose, dopamine and ethylene glycol) followed by the carbonization process.¹⁸⁻²⁰ These approaches led to improved

performance, however, most of the previous approaches adopt relatively complex and expensive synthetic procedures. Thus, synthesis of uniform Fe₃O₄@C nanoparticles with high magnetization, good stability and excellent biocompatibility via green and economical methods still is desirable.

The major challenges in drug delivery are the limited bioavailability, the targeted release of a cargo which can be triggered by a stimulus, and the duration of blood circulation of the cargo load system. A release stimulus that is often used is the pH gradient between the extra- and intracellular regions and between healthy and diseased tissue.²¹ There have been some reports focused on biocompatible nanotransport systems based on magnetic carbon nanocomposites. These nanocomposites are able to load anti-tumor drugs without damaging the payload during load process and can be triggered by a slightly acidic pH to release the load. Recent examples for nanometer-sized magnetic carriers that fulfill these criteria are the Fe₃O₄-graphene composites and graphene-carbon nanotube-Fe₃O₄ hybrid. These two drug-loaded nanocarriers had great water-solubility and the release of the drug was efficient at a mild acidic pH of 4.0. The composites before drug-loading showed negligible cytotoxicity in a control experiment, while drug-loaded nanocarriers retained high anti-tumor activities, which proved the efficient drug release into tumor cells. Drawback of these systems is the low magnetic saturation value as it's just 23 and 19 emu g⁻¹ respectively, which may be not good for magnetic target delivery.^{22,23} Another nano-sized Fe₃O₄@graphene yolk-shell nanoparticles were also used for anticancer drug delivery, which had high drug-loading efficiency and pH-activated release. However, the release process

was too fast to sustain the cargo load system through blood circulation to get to the disease area and just 25% of the loading-drug was released.²⁴ Therefore, a magnetic-carbon hybrid system with effective anticancer drug loading, strong magnetic, pH-stimuli responsive drug release and relative long time duration, as well as other function like great heat generation ability and good biocompatibility would hold great potential in biomedical application.

In this work, we demonstrate the large-scale synthesis of Fe₃O₄@C nanoparticles with uniform size and good dispersity via a simple hydrothermal method. In this reaction, easily operated FeCl₂·4H₂O was chosen as the only source of Fe without any extra addition of oxidants, starch was chosen as carbon source, while not only did NaAc work as base, but as modifier to promote the formation of well-defined core@shell Fe₃O₄@C nanoparticles. In consideration of potential application of our Fe₃O₄@C nanoparticles in biomedicine, their magnetic property and biocompatibility were evaluated. A common anti-cancer drug doxorubicin (DOX) used in the treatment of solid tumor was used for drug-loading and releasing research. Heat generating effect of the prepared samples in alternating magnetic field was also studied in vitro.

Materials and methods

Materials

Ferrous chloride (FeCl₂·4H₂O), sodium acetate (NaAc), starch were purchased from Sinopharm Chemical Reagent Co., Ltd. Minimum essential medium and fetal bovine serum were purchased from Invitrogen (USA). Doxorubicin hydrochloride (DOX), 3-(4,5-dimethylthiazol-2-yl)-2,5-diphenyltetrazolium bromide (MTT) and dimethylsulfoxide (DMSO) were purchased from Sangon Biotech Co., Ltd. (Shanghai, China). All of the reagents were analytical grade and used without further purification unless otherwise indicated. Deionized water was used in the experiments throughout.

Synthesis of Fe₃O₄@C nanoparticles

Fe₃O₄@C nanoparticles with core-shell structure were obtained by one step hydrothermal method. Firstly, 0.5 g of starch, 0.4472 g of FeCl₂·4H₂O and 1.2242 g of NaAc was added into 20 mL of H₂O in a 50 mL three-necked flask. Vigorous mechanical stirring was made for 20 min at 80 °C in a water bath to get a homogeneous solution. Then the solution was transferred into a Teflon-lined stainless steel autoclave (20 mL capacity) for hydrothermal treatment at 200 °C for 20 h. After cooled down to room temperature (R.T.), the black precipitate was collected by a magnet and washed several times with ethanol and water, respectively. The sample was dried overnight at 40 °C before characterization and application.

Characterization of composition and structure of the prepared samples

The morphology of the products was investigated by a transmission electron microscope (TEM, JEM-2100) operated at 200 kV. X-ray diffraction (XRD) patterns were obtained with a Rigaku Ultima IV (D/tex) diffractometer using Cu K α radiation ($\lambda=1.541$ Å). The transmission Mössbauer spectroscopy

experiments were carried out in a constant acceleration with a 25mCi⁵⁷Co(Pb) source at R.T. using 25 μ m α -Fe foil as reference. The Mössbauer parameters were fitted by a standard least-squares fitting program. The Raman spectrum was taken on an inVia Reflex spectrometer (Renishaw) with an argon-ion laser at an excitation wavelength of 514 nm. Mettler Toledo thermogravimetric and differential thermal combined analyzer of type TGA/SDTA 851e was used to check out the thermal performance of the products with the temperature range from 25 to 700 °C at a heating rate of 20 °C min⁻¹ in air atmosphere. Nitrogen adsorption-desorption isotherms were performed by using a Micromeritics ASAP 2010 M analyzer on the dried sample which had been degassed at 80 °C under vacuum for 6 h. The Brunauer-Emmett-Teller (BET) specific surface area was calculated from the linear part of the BET plot. Pore size distribution was calculated using Barrett-Joyner-Halenda (BJH) method. Magnetic hysteresis loops were obtained at R.T. using a Lakeshore 7400 model vibrating sample magnetometer (VSM) under a magnetic field up to 12 kOe. Fourier-transform infrared (FT-IR) spectra were measured in wavenumber ranging from 400 to 4000 cm⁻¹ using Nicolet Nexus 670 FT-IR spectrophotometer. The dried samples were grinded with KBr together, and then compressed into thin pellets for measurement.

Loading of DOX

For drug-loading research, most widely used DOX was chosen as a model drug. In brief, 5 mg of Fe₃O₄@C nanoparticles were dispersed in 20 mL pH 7.4 phosphate buffer solution (PBS, DOX 100 mg L⁻¹). The suspension was shaken at 30 °C, an aliquot of solution was taken out at given intervals and separated with an external magnet. The concentration was obtained on the basis of the standard curve by using a Unico UV-2802S ultraviolet and visible (UV-Vis) spectrophotometer at 480 nm. Adsorption isotherm at 30 °C was also measured in order to ensure the saturated adsorption. DOX solution with different concentration was mixed with Fe₃O₄@C nanoparticles, shaken for 8 hours for total adsorption equilibrium. The absorbance of the solution was measured after magnetic separation. The DOX-loading efficiency of the nanoparticles was judged by q calculated according to the following formula:

$$q = \frac{(C_0 - C)V}{m}$$

Where C_0 is the initial concentration of DOX, C is the concentration of DOX after adsorption, V is the volume of DOX solution, and m is the mass of Fe₃O₄@C nanoparticles.

In vitro drug release

To study drug release, two sets of experiments with different pHs (5.8 and 7.4) were performed at 37 °C. In each drug release experiment, 3.0 mg of DOX loaded Fe₃O₄@C nanoparticles were dispersed in 30 mL PBS with pH of 5.8 or 7.4 in a three-necked, round-bottomed flask, placed the flask in a water bath. The release medium was withdrawn at predetermined time intervals and equal amount of fresh PBS was added at the same time to keep the total solution volume as constant of 30 mL. The samples were analyzed at spectrometer after separation to determine the amount of DOX released.

The cumulative DOX release was calculated by:

$$\text{DOX release (\%)} = \frac{M_t}{M_0} \times 100\%$$

Where M_t is the total amount of DOX released from DOX-loaded $\text{Fe}_3\text{O}_4@\text{C}$ at time t , and M_0 is the amount of DOX initially loaded onto $\text{Fe}_3\text{O}_4@\text{C}$.^{25,26}

Cellular cytotoxicity of DOX-loaded $\text{Fe}_3\text{O}_4@\text{C}$ nanoparticles were conducted by MTT assay as discussed in vitro cytotoxicity assay part with some modification. The DOX loaded nanoparticles diluted in serum-free culture medium were added to the wells at final concentrations of 0.5, 1, 2, 3, 5, 10 and 20 $\mu\text{g mL}^{-1}$ for DOX, respectively.

In vitro cytotoxicity assay

The cell viability was chosen as a cytotoxicity parameter and determined using a colorimetric assay with MTT reagent. The human hepatoma cell line HepG2 was used to evaluate cell viability in the presence of the nanoparticles. The HepG2 cells were grown as monolayer in minimum essential medium supplemented with 10% fetal bovine serum, 100 units ml^{-1} penicillin and 100 $\mu\text{g mL}^{-1}$ streptomycin in a humidified atmosphere containing 5% CO_2 at 37 °C. In the experiments, cells were seeded at a density of 1×10^4 cells per well in 96-well culture plates and incubated for 24 h before adding the nanoparticles. The nanoparticles diluted in serum-free culture medium were added to the cells at indicated concentrations and cultured at 37 °C. 48 hours post incubation, the MTT reagent was added to each well and cells were incubated for an additional 4 h. Then all the mediums were removed and 100 μL of DMSO was added and mixed thoroughly to dissolve formazan crystals. After incubation at 37 °C for 10 minutes, the absorbance of the solubilized formazan product was spectrophotometrically quantified in an ELISA microplate reader at 570 nm with the reference at 630 nm (Bio-tek, Synergy). All experiments were performed three times and in triplicates. The relative cell viability was calculated. For analysis of the biocompatibility, cells were incubated with $\text{Fe}_3\text{O}_4@\text{C}$ and culture medium as a control. For evaluation of the cytotoxicity, cells were treated with DOX-loaded $\text{Fe}_3\text{O}_4@\text{C}$ and used $\text{Fe}_3\text{O}_4@\text{C}$ as a control. Data are expressed as means \pm SD of a representative of three independent experiments performed in triplicate. In all statistical evaluations, $P < 0.05$ was considered as statistically significant.

Magneto-thermal property of $\text{Fe}_3\text{O}_4@\text{C}$ nanoparticles

The heating ability of our $\text{Fe}_3\text{O}_4@\text{C}$ was measured from the time-dependent calorimetric measurements. The aqueous nanoparticles' solution with the concentration of 8 mg mL^{-1} was chosen in this experiment. One milliliter of the sample was taken in a centrifuge tube (2 mL capacity), with suitable arrangements to minimize the heat loss. The RF generator (SP-15A) used for this experiment has a variable field down to 15.1 kA m^{-1} and a fixed frequency of 45 kHz. In this study, AC magnetic fields of 15.1 and 17.4 kA m^{-1} were used.

Results and discussion

Preparation and characterization of $\text{Fe}_3\text{O}_4@\text{C}$

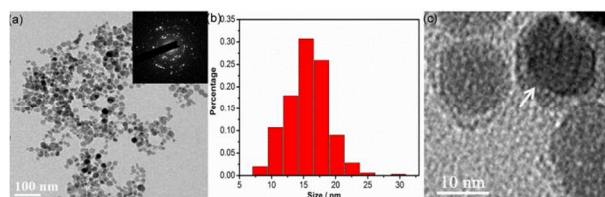


Figure 1. TEM images with different magnification (a, c) and size distribution (b) of $\text{Fe}_3\text{O}_4@\text{C}$.

In order to examine the morphology and architecture of these as-obtained samples, TEM and SAED measurements were conducted. TEM image in Figure 1a shows that the products are composed of well dispersed nanoparticles with irregular shape. Size of these nanoparticles ranges from 8 nm to 30 nm, which centers at 16 nm (Figure 1b). Discreted diffraction dots in SAED picture (inset of Figure 1a) indicate that these nanoparticles are well-crystallized. TEM image of higher magnification in Figure 1c demonstrates that these nanoparticles are of core@shell structures, in which the edge of these particles with light contrast means C as indicated by arrow. This result demonstrated that starches were successfully transformed into carbon under the hydrothermal treatment process and coated on the surface of the magnetite nanoparticles.

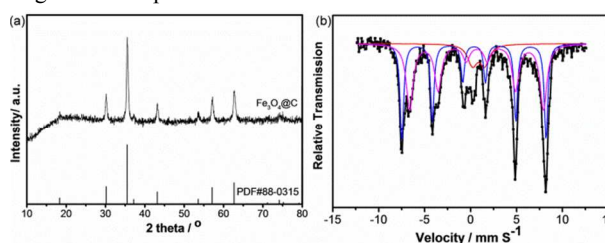


Figure 2. XRD patterns (a) and Mössbauer spectra (b) obtained from $\text{Fe}_3\text{O}_4@\text{C}$ at room temperature.

Table 1. Mössbauer parameters of Fe_3O_4 in $\text{Fe}_3\text{O}_4@\text{C}$.

Sample	Fe component	Isomer shift (mm s^{-1})	Quadrupole Shift (mm s^{-1})	Hyperfine Field (kOe)	Wid	Area ratio
	D	0.69 \pm 0.13	1.49 \pm 0.15	-	0.40 \pm 0.13	0.090 \pm 0.030
$\text{Fe}_3\text{O}_4@\text{C}$	S1	0.37 \pm 0.02	0.02 \pm 0.01	485.84 \pm 0.56	0.23 \pm 0.01	0.412 \pm 0.025
	S2	0.66 \pm 0.04	0.03 \pm 0.03	451.21 \pm 1.32	0.45 \pm 0.02	0.498 \pm 0.034

The components and structures of the samples were determined by powder X-ray diffraction (XRD) and Mössbauer spectroscopy. A typical XRD pattern of the resulted products in Figure 2a shows all peaks are in good agreement with face-centered cubic inverse spinel structure Fe_3O_4 (JCPDS Card No. 88-0315) and no impurities are detected. The diffraction peaks of $\text{Fe}_3\text{O}_4@\text{C}$ have higher background at around 20°, which is due to the presence of amorphous carbon.^{27,28} The average crystallite size was about 19.8 nm for Fe_3O_4 crystal particle in $\text{Fe}_3\text{O}_4@\text{C}$, obtained from Sherrer equation,²⁹ consist with TEM results. Experimental and fitted Mössbauer spectra for $\text{Fe}_3\text{O}_4@\text{C}$ sample at R.T. are discerned in Figure 2b and the hyperfine parameters are tabulated in Table 1. The spectrum of $\text{Fe}_3\text{O}_4@\text{C}$ was best fitted with two sextets and a doublet. The first sextet having hyperfine field (H) 485.84 kOe and isomer shift (I.S.) 0.37 mm s^{-1} is assigned to Fe^{3+} at the tetrahedral (A) site. The other sextet having hyperfine field 451.21 kOe and isomer shift 0.66 mm s^{-1} has been assigned to the

presence of both Fe^{3+} and Fe^{2+} at the octahedral (B) sites. The extra doublet indicates some of Fe_3O_4 in $\text{Fe}_3\text{O}_4@\text{C}$ composite are superparamagnetic at R.T, which may be due to finite size effect caused by the smaller size of Fe_3O_4 in $\text{Fe}_3\text{O}_4@\text{C}$ composite than the critical size.³⁰ Combined with XRD pattern, we can make sure that the samples contain no other iron oxide phase than Fe_3O_4 in the obtained samples.

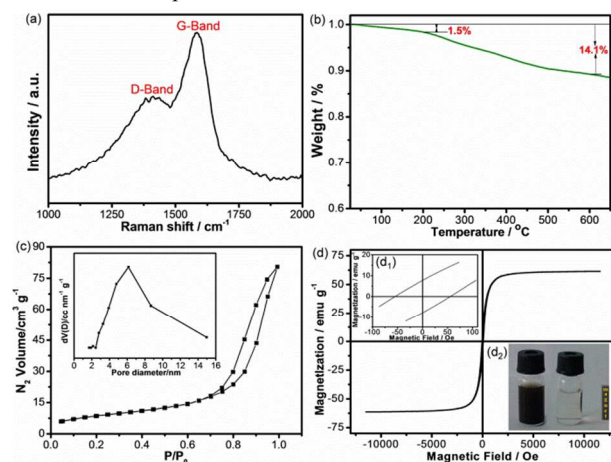


Figure 3. (a) Raman spectrum and (b) TGA curve of $\text{Fe}_3\text{O}_4@\text{C}$ sample; (c) N_2 adsorption–desorption isotherms and pore size distribution of $\text{Fe}_3\text{O}_4@\text{C}$; (d) M-H loop of $\text{Fe}_3\text{O}_4@\text{C}$ nanoparticles at room temperature, inset d₂ shows its great water solubility and magnetic responsiveness.

Raman spectroscopy was also measured to further ascertain the existence of carbon and its crystalline (Figure 3a). The peak at 1396 cm^{-1} is associated with the vibrations of carbon atoms with dangling bonds for the in-plane terminations of disordered graphite that labeled as D-band. The peak at 1585 cm^{-1} is closely related to the vibration in all sp^2 bonded carbon atoms in a two-dimensional hexagonal lattice that labeled as G-band. These two vibrational peaks are broad, and the intensity ration of the two bands (I_D/I_G) reaches as high as 0.76, which indicates the poor crystallinity of carbon in the as-formed state.^{27,31,32} Therefore, the Raman spectrum shows that carbon in our sample is disordered, in agreement with XRD pattern observation. According to TGA analysis (Figure 3b), the total weight loss of $\text{Fe}_3\text{O}_4@\text{C}$ nanoparticles was 14.1%. The 1.5% weight loss below 200 °C was due to the evaporation of water physically adsorbed on the sample, thus only 12.6% weight loss was caused by carbon.^{19,31} That's to say, the carbon content is about 12.6% in the sample. Figure 3c shows the adsorption–desorption isotherm and the pore size distribution curves of $\text{Fe}_3\text{O}_4@\text{C}$. The BET surface area is 34.69 $\text{m}^2 \text{g}^{-1}$ and the pore size distribution reveals a relative narrow pore-size distribution centered at 6 nm.

To investigate the magnetic properties of the $\text{Fe}_3\text{O}_4@\text{C}$ core-shell nanoparticles, magnetic hysteresis loops were recorded at R.T. with an American Lakeshore 7400 vibrating sample magnetometer (VSM). Figure 3d shows the saturation magnetization (M_s) of $\text{Fe}_3\text{O}_4@\text{C}$ is about 61.4 emu g^{-1} , a little smaller than bulk Fe_3O_4 .³³ This could be attributed to the rather smaller size of Fe_3O_4 and the existence of non-magnetism carbon.³² The inset d₁ of Figure 3d shows the remanence (M_r) is 7.7 emu g^{-1} and the coercivity (H_c) is 55 Oe, combined with Mössbauer results, confirm the small size of $\text{Fe}_3\text{O}_4@\text{C}$. However,

the magnetization is large enough not only for separating the sample from the reaction medium rapidly and easily in a magnetic field, but also delivered to the target region by applying a moderate external magnetic field. As shown in the inset d₂ of Figure 3d, the $\text{Fe}_3\text{O}_4@\text{C}$ core-shell nanoparticles dispersed in water to form a uniform stable suspension of black. The black powder was completely attracted within 20 s in the presence of an external magnet, and the solution became transparent. After taking away the magnet and gentle shake, the particles dispersed well into water again. The excellent dispersion ability in water and magnetic response suggest great potential application in biomedicine for our $\text{Fe}_3\text{O}_4@\text{C}$ sample.

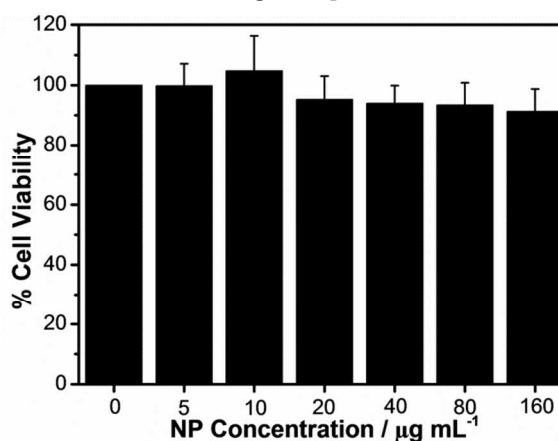


Figure 4. Cell viability of HepG2 cells incubated with different concentrations of $\text{Fe}_3\text{O}_4@\text{C}$ suspensions at 37 °C for 48 hours.

Cytotoxicity of $\text{Fe}_3\text{O}_4@\text{C}$ nanoparticles

For biomedical applications such as drug delivery and magnetic heat therapy, the toxicity is a major concern. To examine the cytotoxicity of $\text{Fe}_3\text{O}_4@\text{C}$, HepG2 cells were incubated with different concentrations of the $\text{Fe}_3\text{O}_4@\text{C}$ nanoparticles for 48 h. MTT assay showed that the nanoparticles had no effects on the growth of HepG2 cells at the concentration range of 5–160 $\mu\text{g mL}^{-1}$ (Figure 4). Even at the highest concentration of $\text{Fe}_3\text{O}_4@\text{C}$ nanoparticles, the relative cell viability was still over 90%. These data indicated that $\text{Fe}_3\text{O}_4@\text{C}$ nanoparticles obtained by our one-step hydrothermal method are biocompatibility.³³

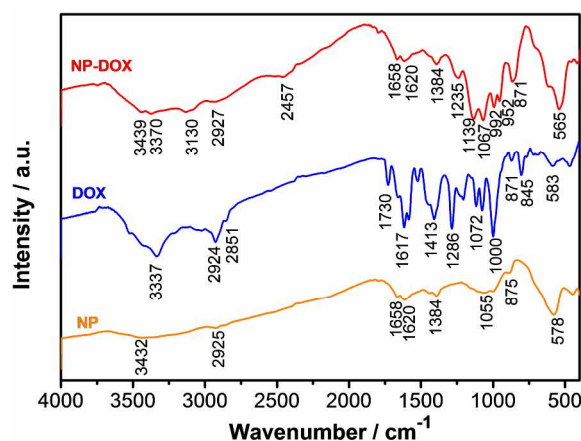


Figure 5. FT-IR spectra of $\text{Fe}_3\text{O}_4@\text{C}$ nanoparticles before (NP) and after drug-loading (NP-DOX), DOX was measured for comparison.

Drug loading capacity of Fe₃O₄@C

The concentration of DOX in the experimental process was obtained on the basis of the standard curve. FT-IR spectra were measured in order to investigate the interaction between DOX and Fe₃O₄@C nanoparticles. Figure 5 shows the IR spectra of Fe₃O₄@C nanoparticles (NP) and after the adsorption of DOX (NP-DOX). For comparison purpose, the characteristic spectrum for pure DOX is also included (DOX). The characteristic absorption band for the Fe-O spinel vibration at 570 cm⁻¹ is observed for nanoparticle spectra (NP, NP-DOX). The adsorption of DOX onto Fe₃O₄@C nanoparticles resulted in a change of the spectrum as shown in Figure 5. Additional bands that can be ascribed to the DOX bands appear at 990-1120 cm⁻¹ and 1210-1290 cm⁻¹. Methylene stretching vibrations at 2851 and 2924 cm⁻¹ and amine stretching at 3337 cm⁻¹ (DOX) are merged with a very broad band in the 2800-3600 cm⁻¹ range, most probably due to the intermolecular hydrogen bonds between the carbon "shell" and adsorbed DOX. The disappearance of a carbonyl asymmetric stretching of DOX (1730 cm⁻¹) perhaps is also due to the above intermolecular interactions.^{26,34} It is also worth noticing that since DOX shows a positive charge in neutral state, which leads to a strong interaction with the negatively charged Fe₃O₄@C through the robust electrostatic attraction. Thus, the high negative charge density of Fe₃O₄@C helped them load a considerable amount of DOX as well as improve their stability in solution.

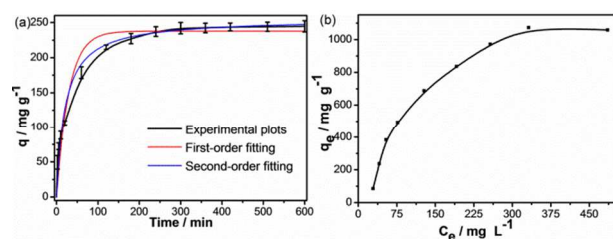


Figure 6. (a) Adsorption equilibrium curve of DOX onto Fe₃O₄@C and fitting with kinetic models; (b) Adsorption isotherm for the Fe₃O₄@C drug loading process.

Table 2. Kinetic models and parameters fitting results for the adsorption of DOX.

Kinetic Model Equation	Kinetic Model Parameters	Nonlinear analysis
pseudo-First-order		
	$k_1 / (\text{min}^{-1})$	3.3930×10^{-2}
$q_t = q_m(1 - e^{-k_1 t})$	$q_m(\text{theo}) / (\text{mg g}^{-1})$	237.8266
	$q_e(\text{exp}) / (\text{mg g}^{-1})$	247.9210
	R^2	0.9544
pseudo-Second-order		
	$k_2 / (\text{g mg}^{-1} \text{min}^{-1})$	0.1911×10^{-3}
$q_t = k_2 q_m^2 t / (1 + k_2 q_m t)$	$q_m(\text{theo}) / (\text{mg g}^{-1})$	255.7612
	R^2	0.9797

As the drug loading process was an adsorption process, we not only studied the adsorption equilibrium curve to make sure the equilibrium time, but also the adsorption isotherm to find saturate adsorption content at 30 °C. From Figure 6a, we can see the process almost reached equilibrium in just 6 h, thus we did the following experiments for 8 h to ensure totally adsorption

equilibrium. The amount of drug loaded into the nanoparticles was shown in Table 2, which was 247.9 mg g⁻¹. The drug-loading percentage was calculated according to the following formula:

$$\text{Drug loading percentage} = \frac{m_{\text{added DOX}} - m_{\text{unbound DOX}}}{m_{\text{added DOX}}} \times 100\%$$

and the value turned out to be 61.8%. In order to elucidate the adsorption mechanism, the kinetics data were fitted using two different models. Comparison between the experimental adsorption data and the theoretical values is illustrated in Figure 6a and the obtained parameters are given in Table 2. According to Table 2, the value of $q_m(\text{theo})$ for the pseudo-second-order kinetics model is closer to $q_e(\text{exp})$ than the value of $q_m(\text{theo})$ for the pseudo-first-order kinetics model. In addition, the correlation coefficient (R^2) for the pseudo-second-order kinetics model is higher than that of the pseudo-first-order kinetics model. These results indicate that the pseudo-second order kinetic model can effectively describe the observed kinetics. To determine the saturation level of DOX onto our Fe₃O₄@C nanoparticles, Fe₃O₄@C nanoparticles were added into pH 7.4 PBS solutions with different concentrations of DOX. As shown in Figure 6b, the equilibrium adsorption capacity of DOX onto Fe₃O₄@C nanoparticles increased with the increase of DOX concentration. The highest equilibrium adsorption capacity reached 1079.82 mg g⁻¹, much higher than the other drug carriers.²⁶

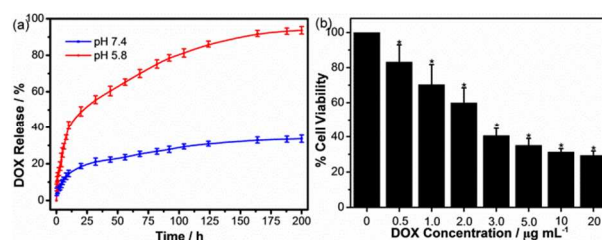


Figure 7. (a) Drug-release kinetic curves obtained at different pH; (b) The cell viability of HepG2 cells treated with different concentrations of DOX loaded by Fe₃O₄@C nanoparticles for 48 h. *P < 0.05, compared to Fe₃O₄@C.

In vitro drug release kinetics and cytotoxicity of NP-DOX

Figure 7a displays the cumulative release profile of DOX as a function of time under different conditions (pH 7.4 means physiological condition, while pH 5.8 mimics slightly acidic environment of tumors³⁵). Both of the systems show a sustained drug release pattern as expected, and the drug released ration of weak acid system is significantly higher than neutral, indicating the pH-sensitive drug release mechanism of our Fe₃O₄@C nanoparticles. About 48.1% of DOX was released in 20 h in pH 5.8 PBS, while only 18.7% was released in pH 7.4 system. As prolonging the incubation time to 200 h, nearly 93.7% DOX was released in acid system while 33.6% in neutral. It was thought that the more drug release was triggered by the impairment of the interaction between DOX and the nanoparticles, including cleavage of the hydrogen bond and disappearance of electrostatic interaction under the acid condition. As we know, the acidity is always stronger in tumor site than normal tissues, when the drug-load particles reach the targeted tumor site, more drug would be released under the stimulation of lower pH.^{29,36} Utilizing the pH-

dependent drug release superiority, $\text{Fe}_3\text{O}_4@\text{C}$ nanoparticles can reserve part of DOX before getting to the cancer cells, which can enhance circulation time and drug retention in the blood circulation system. Additionally, instead of the burst release, the consecutive and gradual release profiles were observed at the whole stage as long as 200 h, this is quite good for clinical cancer treatment. The pH-sensitive and long-time gradual release feature of the drug release process is quite beneficial for more efficient tumor-target therapy with negligible side-effect. We measured the magnetic hysteresis loops of the $\text{Fe}_3\text{O}_4@\text{C}$ nanoparticles after drug release at pH 5.8 for 200 h to prove the stable magnetic property of the sample. As shown in Figure S1 in the supplementary information, the saturation magnetization (M_s) still reached 55.6 emu g^{-1} , just decreased a little compared with the $\text{Fe}_3\text{O}_4@\text{C}$ nanoparticles before drug loading (61.4 emu g^{-1}). This result clearly demonstrated our $\text{Fe}_3\text{O}_4@\text{C}$ nanoparticles could overcome the drawback of poor magnetic saturation of the sample during long-term drug-releasing process.

In order to evaluate the cytotoxicity of drug-loaded $\text{Fe}_3\text{O}_4@\text{C}$ nanoparticles, we treated HepG2 cells with $\text{Fe}_3\text{O}_4@\text{C}$ nanoparticles in the absence or presence of indicated concentrations of DOX for 48 h. As shown in Figure 7b, the NP-DOX lowered the cell viability in a dose-dependent manner. 17% decrease was detected with DOX concentration at $0.5 \mu\text{g mL}^{-1}$ and a maximal 70% inhibition was found at $10 \mu\text{g mL}^{-1}$ ($P < 0.05$ and $P < 0.01$, respectively). As we know, cells only die when DOX chelates with DNA inside the nucleus and arrest the cell functions.³⁷ The prominent cytotoxicity of the NP-DOX implied an efficient cellular uptake of drug from our drug-loading nanoparticles. Since the DOX is linked to the $\text{Fe}_3\text{O}_4@\text{C}$ nanoparticles through hydrogen bonds and electrostatic interactions, once the drug-loaded nanoparticles entered into the cell, the DOX is easily released from the NP-DOX under the chemical environment within the cytoplasm and is available to penetrate within the nucleus of the cell to kill the cell by chelating with DNA.³⁸ In addition, although a small amount of drug was also released before NP-DOX entered the cells, the acidic extracellular environment can promote the released drug diffusing through the cell membrane into the intracellular compartment to kill the cancer cells.^{39,40,41} Together with great biocompatibility, the efficient anti-cancer efficiency after drug loading the $\text{Fe}_3\text{O}_4@\text{C}$ nanoparticles have potential cancer treatment applications.

45 Magneto-thermal property of $\text{Fe}_3\text{O}_4@\text{C}$ nanoparticles

The temperature variation with time of magnetic treatment in Figure 8 explored the heat generating effect of $\text{Fe}_3\text{O}_4@\text{C}$. In a magnetic field of 15.1 kA m^{-1} , temperature of the magnetic solution increased to $55.2 \text{ }^\circ\text{C}$ in 30 min. It's just need 6 min to get $45.0 \text{ }^\circ\text{C}$, which is an effective and appropriate temperature for the localized hyperthermia treatment of cancer, but has little side effect to human normal cells. Magnetic heat-generation was further tailored by improving the magnetic field strength. When the field strength improved to 17.4 kA m^{-1} , the temperature would reach $45.0 \text{ }^\circ\text{C}$ in less than 4 min, and up to a high temperature as $72.4 \text{ }^\circ\text{C}$ in 30 min. For ferromagnetic nanoparticles, sufficient heat would be produced by hysteresis loss when they were placed

in an alternating magnetic field of high frequency, which depends upon the existence of coercive force and remanence magnetization.⁴² However, as some of the $\text{Fe}_3\text{O}_4@\text{C}$ nanoparticles are superparamagnetic as we learned from the Mössbauer results, the magnetic heat generation may also partly be caused by Néel and Brownian relaxations.^{43,44}

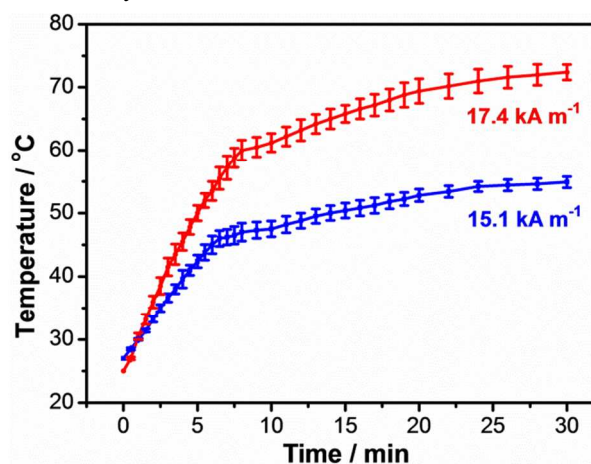


Figure 8. Temperature kinetic curves obtained after application of an alternating magnetic field on the samples dispersed in water with a concentration of 8 mg mL^{-1} .

Conclusions

A new facile one-step hydrothermal strategy has been demonstrated for fabricating $\text{Fe}_3\text{O}_4@\text{C}$ nanoparticles that exhibit good dispersity, quick magnetic responsibility and great biocompatibility. Composition and surface analyses have proven that the resulted nanoparticles consist of the Fe_3O_4 core and the C shell. This simple method may be extended to the synthesis of other nanoparticles/carbon composites. In the multifunctional nanoparticles, the magnetic Fe_3O_4 core could be easily controlled by external magnetic field and used to generate heat in AC magnetic field. The existence of C made the material achieve high loading efficiency of DOX, and the duration release of the drug from this hybrid was much higher under acid conditions compared with neutral conditions. Thus, our multifunctional $\text{Fe}_3\text{O}_4@\text{C}$ nanoparticles have great potential in future cancer theranostic applications.

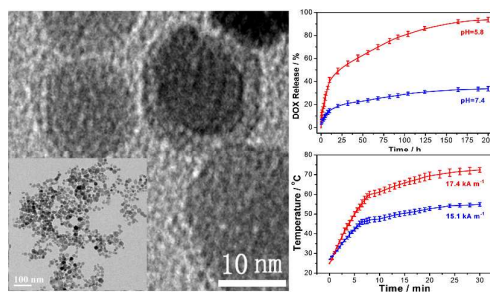
85 Acknowledgements

This work was supported by the National Natural Science Foundation of China (Grant No. 21173084) and Large Instruments Open Foundation of East China Normal University.

90 Notes and references

- ^a Department of Physics, Center for Functional Nanomaterials and Devices, East China Normal University, Shanghai 200241, P. R. China. E-mail: jsjiang@phy.ecnu.edu.cn (J. S. Jiang); Fax/Tel: +86-21-54342940
- ^b Shanghai Diabetes Institute, Shanghai Key Laboratory of Diabetes Mellitus, Department of Endocrinology and Metabolism, Shanghai Jiao Tong University Affiliated Sixth People's Hospital, Shanghai 200233, P. R. China. E-mail: qefang@sytu.edu.cn (Q. C. Fang); Fax/Tel: +86-21-24058657
- ^c Engineering Research Center of Advanced Glasses

- Manufacturing Technology, MOE, Donghua University, Shanghai 201620, P. R. China*
- 1 A. A. Date and C.J. Destache, *Biomaterials*, 2013, **34**, 6202-6228.
- 2 J. Kim, Y. Piao and T. Hyeon, *Chem. Soc. Rev.*, 2009, **38**, 372-390.
- 3 Y. Yang, J. S. Jiang, B. Du, Z. F. Gan, M. Qian and P. Zhang, *J. Mater. Sci. : Mater. Med.*, 2009, **20**, 301-307.
- 10 4 Y. Xu, W. E. Heberlein, M. Magmood, A. I. Orza, A. Karmakar, T. Mustafa, A. R. Biris, D. Casciano and A. S. Biris, *J. Mater. Chem.*, 2012, **22**, 20128-20142.
- 5 E. Kim, K. Lee, Y. M. Huh and S. Haam, *J. Mater. Chem. B*, 2013, **1**, 729-739.
- 15 6 L. Gao, L. Xie, X. Long, Z. Wang, C. Y. He and B. Qiu, *Biomaterials*, 2013, **34**, 3688-3696.
- 7 B. Zhang, B. Yang, C. Zhai, B. Jiang and Y. Wu, *Biomaterials*, 2013, **34**, 5843-5852.
- 8 M. Das, P. Dhak, S. Gupta, D. Mishra, T. K. Maiti, A. Basak and P. Pramanik, *Nanotechnology*, 2010, **21**, 125103-125115.
- 20 9 A. K. Gupta and Gupta M, *Biomaterials*, 2005, **26**, 3995-4021.
- 10 P. B. Santhosh and N. P. Ulrih, *Cancer Lett.*, 2013, **336**, 8-17.
- 11 P. Liu, L. Qin, Q. Wang, Y. Sun, M. Zhu, M. Shen and Y. Duan, *Biomaterials*, 2012, **33**, 6739-6747.
- 25 12 S. Mornet, S. Vasseur, F. Grasset and E. Duguet, *J. Mater. Chem.*, 2004, **14**, 2161-2175.
- 13 T. Zhou, B. Wu and D. Xing, *J. Mater. Chem.*, 2012, **22**, 470-477.
- 14 X. Li, X. Huang, D. Liu, X. Wang, S. Song, L. Zhou and H. Zhang, *J. Phys. Chem. C*, 2011, **115**, 21567-21573.
- 30 15 J. S. Jiang, Z. F. Gan, Y. Yang, B. Du, M. Qian and P. Zhang, *J. Nanopart. Res.*, 2009, **11**, 1321-1330.
- 16 Z. F. Gan, J. S. Jiang, Y. Yang, B. Du, M. Qian and P. Zhang, *J. Biomed. Mater. Res. A*, 2008, **84A**, 10-18.
- 35 17 R. Zhang and H. Olin, *Mater. Sci. Eng. C*, 2012, **32**, 1247-1252.
- 18 Z. Wang, H. Guo, Y. Yu and N. He, *J. Magn. Magn. Mater.*, 2006, **302**, 397-404.
- 19 C. Lei, F. Han, D. Li, W. C. Li, Q. Sun, X. Q. Zhang and A. H. Lu, *Nanoscale*, 2013, **5**, 1168-1175.
- 40 20 Q. Zhang, Z. Shi, Y. Deng, J. Zheng, G. Liu and G. Chen, *J. Power Sources*, 2012, **197**, 305-309.
- 21 S. Nowag and R. Haag, *Angew. Chem. Int. Ed.*, 2014, **53**, 49-51.
- 45 22 X. Fan, G. Jiao, W. Zhao, P. Jin and X. Li, *Nanoscale*, 2013, **5**, 1143-1152.
- 23 X. Fan, G. Jiao, L. Gao, P. Jin and X. Li, *J. Mater. Chem. B*, 2013, **1**, 2658-2664.
- 24 S. Li, J. Zheng, D. Chen, Y. Wu, W. Zhang, F. Zheng, J. Cao, H. Ma and Y. Liu, *Nanoscale*, 2013, **5**, 11718-11724.
- 50 25 T. Ren, Q. Liu, H. Lu, H. Liu, X. Zhang and J. Du, *J. Mater. Chem.*, 2012, **22**, 12329-12338.
- 26 J. Chen, Z. Guo, H. B. Wang, M. Gong, X. K. Kong, P. Xia and Q. W. Chen, *Biomaterials*, 2013, **34**, 571-581.
- 55 27 S. M. Yuan, J. X. Li, L. T. Yang, L. W. Su, L. Liu and Z. Zhou, *ACS Appl. Mater. Inter.*, 2011, **3**, 705-709.
- 28 Y. Zhu, Y. J. Bai, F. D. Han, Y. X. Qi, N. Lun, B. Yao and J. X. Zhang, *Mater. Lett.*, 2011, **65**, 3157-3159.
- 29 A. Akbarzadeh, M. Samiei, S. W. Joo, M. Anzaby, Y. Hanifehpour, H. T. Nasrabadi and S. Davaran, *J. Nanobiotechnology*, 2012, **10**, 46.
- 60 30 N. N. Song, H. T. Yang, X. Ren, Z. A. Li, Y. Luo, J. Shen, W. Dai, X. Q. Zhang and Z. H. Cheng, *Nanoscale*, 2013, **5**, 2804-2810.
- 65 31 S. Xuan, L. Hao, W. Jiang, X. Gong, Y. Hu and Z. Chen, *Nanotechnology*, 2007, **18**, 035602-035608.
- 32 J. Zhang, J. Du, Y. Qian, Q. Yin and D. Zhang, *Mater. Sci. Eng. B*, 2010, **170**, 51-57.
- 33 S. R. Lenibel, M. L. Moises, C. Cristina, M. V. Janet, L. E. Magda, J. J. Eduardo, M. Edna, T. L. Madeline and R. Carlos, *J. Mater. Chem. B Mater Biol Med.*, 2013, **1**, 2807-2817.
- 70 34 N. Krzysztof, R. Jerzy, K. Krzysztof, S. Jacek, T. Andrzej, M. Maciej and K. Pawel, *J. Phys. Chem. C*, 2012, **116**, 5598-5609.
- 35 W. Y. Qian, D. M. Sun, R. R. Zhu, X. L. Du, H. Liu and S. L. Wang, *Int. J. Nanomedicine*, 2012, **7**, 5781-5792.
- 75 36 W. F. Ma, K. Y. Wu, J. Tang, D. Li, C. Wei, J. Guo, S. L. Wang and C. C. Wang, *J. Mater. Chem.*, 2012, **22**, 15206-15214.
- 37 M. I. Majeed, Q. Lu, W. Yan, Z. Li, I. Hussain, M. N. Tahir, W. Tremel and B. Tan, *J. Mater. Chem. B*, 2013, **1**, 2874-2884.
- 80 38 Y. J. Gu, J. Cheng, C. W. Man, W. T. Wong and S. H. Cheng, *Nanomedicine: NBM*, 2012, **8**, 204-211.
- 39 X. Yu, X. Yang, S. Horte, J. N. Kizhakkedathu and D. E. Brooks, *Biomaterials*, 2014, **35**, 278-286.
- 40 S. C. Offerman, A. V. K. Verma, B. A. Telfer, D. A. Berk, D. J. Clarke and H. S. Aojula, *RSC Adv.*, 2014, **4**, 10779-10790.
- 85 41 L. E. Gerweck, S. Vijayappa and S. Kozin, *Mol. Cancer Ther.*, 2006, **5**, 1275-1279.
- 42 S. A. Shah, M. U. Hashmi, S. Alam and A. Shamim, *J. Magn. Magn. Mater.*, 2010, **322**, 375-381.
- 90 43 S. A. Shah, A. Majeed, K. Rashid and S. U. Awan, *Mater. Chem. Phys.*, 2013, **138**, 703-708.
- 44 T. Sadhukha, T. S. Wiedmann and J. Panyam, *Biomaterials*, 2013, **34**, 5163-5171.



Core@shell structured Fe₃O₄@C nanoparticles synthesized by one-pot hydrothermal method show good pH-response drug release property and magneto-thermal performance.